Talanta 311 (2027) 130201

Contents lists available at ScienceDirect

Talanta

journal homepage: www.elsevier.com/locate/talanta

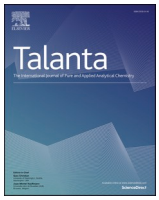

Pixel-wise assessment of industrial compost transformation by NIR hyperspectral imaging and chemometrics: an early-warning tool for process monitoring

Marta P. Rueda [a], Antoine Deryck [b], François Stevens [b], Juan Antonio Fernández Pierna [b], Vincent Baeten [b], María José Ayora-Cañada [a,*], Ana Domínguez-Vidal [a]

[a] Department of Physical and Analytical Chemistry, Universidad de Jaén, Campus Las Lagunillas, Jaén, E-23071, Spain
[b] Valorisation of Agricultural Products Department, Quality and Authentication of Products Unit, Walloon Agricultural Research Centre, Henseval Building, 24 Chaussée de Namur, Gembloux, B-5030, Belgium

ARTICLE INFO

Keywords:
NIR hyperspectral imaging
Pixel-wise PLS-DA
Olive mill pomace composting
Process monitoring
Organic matter degradation

ABSTRACT

Ensuring reliable monitoring of industrial composting remains challenging due to feedstock heterogeneity and the limited representativeness of point-based spectroscopy. Here, near-infrared hyperspectral imaging (NIR-HSI) combined with multivariate modelling was applied for the first time to characterize an industrial olive mill waste composting process. By sampling across different zones of open windrow piles over two campaigns (spanning 2–59 weeks), partial least squares (PLS) regression models were developed to predict key quality indicators (pH, electrical conductivity, C/N ratio, and organic matter content). The models demonstrated satisfactory performance (Residual Prediction Deviation, RPD = 2.4–3.1). Pixel-wise application of PLS models generated spatially resolved prediction maps, revealing localized differences in degradation dynamics that would likely be overlooked by conventional analytical methods. Furthermore, a pixel-wise PLS-DA strategy was implemented to characterise compositional changes throughout composting. In contrast to the quantitative regression models, this approach identified spectral patterns reflecting the progressive breakdown and transformation of the organic matter, providing insights into compost evolution without the need for reference analysis. The PLS-DA model demonstrated an overall accuracy of 94 %, and the Variable Importance in Projection scores indicated wavelengths associated with nitrogen-containing and aromatic structures as relevant maturation indicators. Classification maps captured the gradual decomposition of the initial substrates and compost homogenization. Calculating class-specific pixels (initial raw materials and finished compost) enabled the construction of relative abundance curves reflecting process evolution. Overall, this NIR-HSI workflow opens new possibilities for compost monitoring reliability and represents a promising basis for future data-driven control strategies in heterogeneous biological processes.

1. Introduction

Monitoring the quality of heterogeneous biological processes (such as composting, anaerobic digestion, wastewater treatment or biogas production) remains a significant analytical challenge [1]. Conventional reference methods are often destructive, laborious, time-consuming, and not environmentally friendly, yielding insufficient information to fully capture the intrinsic variability of these systems, where composition can vary substantially even within the same batch [2]. As a result, real-time quality assessment is hindered. Therefore, discrete sampling may not provide representative information in large-scale bioreactors or windowed composting piles, and conventional chemical analyses may struggle to adequately describe such variability. Consequently, there is an imperative need for the implementation of rapid, non-destructive analytical techniques that can effectively handle such complex and heterogeneous samples, capable of providing real-time insights into the process dynamics.

In recent years, spectroscopic methods have garnered attention as effective alternatives for these purposes. In particular, near-infrared (NIR) spectroscopy is widely used due to its speed and non-invasive

* Corresponding author.
E-mail address: mjayora@ujaen.es (M.J. Ayora-Cañada).

https://doi.org/10.1016/j.talanta.2026.130201
Received 6 March 2026; Received in revised form 5 June 2026; Accepted 22 June 2026
Available online 23 June 2026

nature [3]. However, it provides a single averaged spectrum per sample, masking internal heterogeneity and preventing visualization of component distribution [4]. In the context of composting or other bioprocesses, traditional NIR instruments are unable to detect significant local variations, such as hotspots of moisture, undecomposed residues or contaminants.

To overcome these limitations, imaging tools have been integrated with NIR spectroscopy to capture both spectral and spatial information. Hyperspectral imaging (HSI) combines the strengths of imaging and spectroscopy by acquiring a complete spectrum for each pixel of the scene under investigation, generating a three-dimensional data cube (or hypercube) with two spatial dimensions (x, y) and one spectral dimension (λ) [5]. HSI in the short-wave infrared (SWIR) range, typically between 1000 and 2500 nm, is particularly effective for organic materials, as most key chemical bonds display distinctive absorption bands in this region [6]. Based on pixel-by-pixel spectral measurements, a complete map is generated with chemical information that allows the distribution of the material's constituents or quality attributes to be visualised. The resulting datasets, typically containing hundreds of thousands of spectra, require multivariate and machine learning methods to extract meaningful information and support both quantitative and qualitative analysis. These analyses allow interpretation based on the underlying chemical constituents of the samples, which exhibit different physicochemical properties. Consequently, the combination of HSI with chemometrics has supported applications in fields like food quality control, agriculture, and soil science, revealing spatial patterns and features (e.g., adulteration, disease spots) that are undetectable by conventional NIR analysis [7–11].

Despite its widespread use in the analysis of food and agricultural products, HSI remains underexplored for monitoring dynamic bioprocesses, especially under industrial conditions. Its potential for non-invasive tracking of temporal and spatial change in chemical composition renders it highly attractive for such applications. To date, only a limited number of studies have demonstrated the capacity of this technique to monitor complex biological transformations through spatially resolved chemical mapping, such as fermentation [12] or microbial growth [13]. Among these, the composting of organic materials represents a paradigmatic example of a large-scale, highly dynamic system that has not yet been fully explored. To the best of our knowledge, no direct applications of hyperspectral imaging combined with chemometric modelling have been reported in the context of composting, which is characterised by spatial gradients of temperature, moisture and microbial activity.

In particular, the co-composting of olive mill pomace, the primary by-product of the olive oil industry, together with other agricultural and livestock waste, presents notable analytical challenges. The matrix is chemically complex, containing a wide range of organic and mineral compounds that evolve both spatially and temporally during composting. At the same time, this co-composting process is of considerable environmental and industrial importance, as it supports the valorisation of agro-industrial residues and contributes to sustainable waste management, playing a relevant role in circular economy strategies for the olive oil sector [14].

In this context, the combination of hyperspectral imaging and chemometric modelling offers a promising strategy for monitoring complex composting systems. Compost quality is commonly evaluated using key physicochemical maturity indicators, such as organic matter content (often expressed as loss-on-ignition, LOI), the carbon-to-nitrogen (C/N) ratio, pH and electrical conductivity (EC), which together reflect organic matter stabilisation, nutrient availability and overall compost maturity.

This work presents, to the best of our knowledge, the first reported application of an integrated HSI-chemometrics strategy for the quantitative and qualitative monitoring of industrial olive mill pomace composting systems, establishing an analytical framework that can be transferred to other complex bioprocesses where spatial variability plays a critical role. By enabling the spatially resolved monitoring of compositional and physicochemical transformations over time through pixel-wise prediction tools, namely partial least squares discriminant analysis (PLS-DA) and partial least squares (PLS) regression, this strategy bridges analytical chemistry and process monitoring, highlighting the potential of hyperspectral chemometrics to support improved decision-making in industrial system management.

2. Material and methods

2.1. Composting of olive mill pomace and sampling strategy

Compost samples were provided by INGNIA S.L., a composting facility located in Almedinilla (Córdoba, Spain). Composting was conducted in large-scale open windrow piles of approximately 80 m long, 4 m high and 6 m width (Fig. S1a). Each pile was gradually formed during the olive oil production campaign through successive additions of fresh feedstock. The feedstock mixture was typically composed of 60-70 % olive mill pomace (OMP) sourced from local olive mills; 15-25 % goat manure with straw bedding (GM); 5-10 % olive tree pruning residue (OTP), and 1-3 % chicken manure with sawdust bedding (CM) as input materials. Once completed, aeration was maintained by monthly mechanical turning.

As a sampling strategy, each pile was arbitrarily divided into 4 sectors of 20 m in length (S1 to S4), reflecting its progressive growth (Fig. S1b and S1c). As the pile was progressively constructed through successive additions of feedstock, sectors became available over time. Therefore, S1 was present from the beginning of the process, whereas S2, S3 and S4 appeared sequentially as the pile length increased. At each sampling time, two independent composite samples (≈1 kg) were collected from each available sector. Each sample consisted of five thoroughly mixed sub-samples randomly collected at different heights and depths within the corresponding sector. Overall, a total of 126 samples were collected over two consecutive olive harvest seasons, representing compost with maturation times ranging from 2 to 49 weeks in 2020/2021 and from 3 to 59 weeks in 2021/2022. All samples, including compost and the individual raw materials, were oven-dried at 65 °C for 48-72 h (up to constant weight) prior to analysis and stored in sealed bags to minimize exposure to ambient humidity. For each collected sample, separate portions were used for physical-chemical characterization and hyperspectral imaging.

2.2. Physical-chemical characterization

Electrical conductivity at 25 °C (EC) and pH were measured in water extracts according to standard procedures for compost analysis [15]. These extracts (1:10, w/v) were prepared from previously dried compost samples and analysed using an EC-meter CRISON Basic 30 (HACH LANGE, Spain) and a HANNA pH meter (HANNA® Instruments, Australia), respectively. For carbon and nitrogen determination and organic matter estimation via the “loss-on-ignition” (LOI) method, the dried compost was further finely ground in a domestic dry grinder and sieved to 200 µm. C and N analysis was conducted in a LECO TruSpec CHN 620-100-400 (LECO Corporation, USA) elemental analyser while LOI determination involved combustion in a muffle furnace at 550 °C for 5 h [16].

2.3. Near infrared hyperspectral image acquisition

Data acquisition was performed under stable indoor laboratory conditions using an imaging system (SpectralPartners, Haarlem, The Netherlands) combining the Specim SWIR hyperspectral camera (Specim, Spectral Imaging Ltd., Oulu, Finland), equipped with a cryogenically cooled mercury-cadmium-telluride (MCT) detector (XENICS NV, Leuven, Belgium), and a motorized conveyor belt (RMA Techniek, 's-Heer Arendskerke, The Netherlands). The system covered the SWIR range, from 1000 to 2500 nm, with a spectral resolution of 5.6 nm and a

spatial resolution of 0.62 mm/pixel. The camera operated in a push-broom, line-scanning configuration with 384 pixels by line, and a sample translation speed of 74 mm s^{-1}. Illumination was provided by two 150 W halogen lamps positioned at a 45° angle to the sample surface. Dried samples were analysed, without any additional treatments, in order to preserve their intrinsic heterogeneity. Approximately 15 g of compost were spread over a black fabric sheet, forming a compact circle of approximately 10 cm in diameter. The sheet was placed on the conveyor belt to minimize background interference and ensure uniform illumination. Prior to each measurement, the system was calibrated with a dark reference by closing the lenses and a white reference using a Teflon® sheet. To improve the signal-to-noise ratio, the mean spectra of 32 successive scans were averaged per pixel and saved in standard hyperspectral data cube format. Near-infrared hyperspectral images (NIR-HSI) were acquired as three-dimensional datacubes (x, y, λ), where x and y correspond to the spatial dimensions and λ to the spectral dimension, comprising absorbance values (log 1/R) measured at 272 wavelengths. In this configuration, x corresponds to the number of pixels per line (384), while y represents the scan direction, with an average of about 550 lines per datacube. Instrument control and data acquisition were performed with Prediktera Breeze software (Prediktera AB, Umeå, Sweden).

2.4. Construction of NIR-HSI spectral library

A two-dimensional spectral dataset was extracted from each acquired hyperspectral datacube as follows. First, K-means clustering [17] was used to create a mask that removed most of the non-sample features from the obtained HSI images. The algorithm was set to three clusters ($k = 3$), corresponding to the three materials involved in each acquisition setup: the conveyor belt, the supporting black fabric sheet, and the compost sample. The number of clusters was previously defined based on this known composition, and the resulting clustering was visually inspected to ensure correct identification of the compost region prior to mask generation.

The obtained dataset was then subjected to a two-stage cleaning process. Initially, the individual spectra were smoothed using a Savitzky–Golay filter [18] (window length: 21 spectral points; polynomial degree: 2), after which first- and second-order derivatives were calculated. A spike was identified when the absolute values of both derivatives at any point simultaneously exceeded five times their respective mean absolute values [19]. When spikes were detected, the corresponding spectra were excluded from further analysis in order to prevent potential artefacts introduced by spectral reconstruction. Subsequently, the Local Outlier Factor (LOF) algorithm was applied: spectra of pixels that deviated significantly from their k-nearest neighbours (k was set to 20) were identified as outliers and removed [20].

2.5. Chemometrics

All chemometric models were developed using the Python software version 3.11.12 with the PLSRegression module of scikit-learn, implemented in the open-source Spyder integrated development environment (IDE, Spyder Website Contributors).

2.5.1. Partial least squares (PLS) regression

For quantitative modelling, partial least squares (PLS) regression was used to develop predictive models based on a limited number of orthogonal latent variables (LVs), derived from the original spectral data. Mean spectra extracted from the hyperspectral images of the 126 compost samples, covering the full composting process, were used as predictors for PLS regression. Reference values for organic matter content expressed as loss-on-ignition (LOI), carbon-to-nitrogen ratio (C/N), pH, and electrical conductivity (EC), were determined following standard analytical procedures. The dataset was first randomly split into a calibration set (80 % of the compost samples) and a test set (20 %). A detailed description of the statistical distribution of reference values, including mean, range and standard deviation for each parameter is provided in P. Rueda et al. [21].

Separate PLS models were built for each compost quality parameter. For all models, both the preprocessing and the number of LVs were optimised independently by repeated 10-fold cross-validation (five repetitions). The preprocessing strategies evaluated included combinations of one or two methods among standard normal variate (SNV), Savitzky-Golay second-order derivative (polynomial order: 2; window length: 21 spectral points), and linear detrending.

To assess the performance of the models, the calibration (R^2 cal) and prediction (R^2 pred) coefficients of determination, as well as the mean square error of calibration (RMSEC) and prediction (RMSEP) were calculated using the mean spectra of the calibration and test samples. Moreover, the Residual Prediction Deviation (RPD) was calculated as the ratio between the standard deviation of the prediction set and the RMSEP. RPD values between 2 and 2.5 makes approximate quantitative predictions possible. For values between 2.5 and 3.0, and above 3, the prediction is classified as good and excellent, respectively [22]. Once validated, the optimised PLS models developed were applied to all compost hyperspectral images to generate pixel-by-pixel prediction maps.

2.5.2. Partial least squares discriminant analysis (PLS-DA)

PLS-DA models were developed to classify hyperspectral pixels into five target classes, corresponding to the four raw materials (OMP, OTP, GM and CM) and a high-quality compost representative of the final stage of the process (COMP; 33 weeks of composting). The inclusion of this class allowed the evaluation of the spectral convergence of the raw materials towards the targeted end-product state during composting.

The calibration dataset was built from hyperspectral images of these five materials (1 image per material). A dataset comprising 20,000 spectra x 272 wavelengths was generated from randomly selecting 4000 pixels by hyperspectral image for each class to ensure comparable representation during model development. In this case, modelling was performed at the pixel level, where each pixel spectrum was treated as an individual observation. Prior to modelling, spectral data were pre-processed using the standard normal variate (SNV) followed by linear detrending. The optimal number of latent variables (LVs) was determined by repeated 10-fold cross-validation with five repetitions, selecting the model that minimised the classification error. Variable Importance in Projection (VIP) scores were computed for each class, with values above one indicating significant spectral contributions [23].

The confusion matrix and class-wise performance metrics (sensitivity, specificity and F1-score) were used to evaluate the PLS-DA models. These metrics were subsequently analysed on a class-wise basis to provide a more detailed assessment of classification behaviour for individual classes.

For a given class, sensitivity refers to the proportion of pixels of this class that are correctly classified as such. Similarly, specificity indicates the proportion of the pixels not belonging to this class that are also correctly classified as such. The F1-score, defined as the harmonic mean of precision and sensitivity, was included as a complementary metric to provide a concise and robust summary of classification performance.

For external validation of the model, additional hyperspectral measurements were acquired from new samples not included in the calibration dataset, comprising both individual raw materials (three of each) and three mixtures of prepared by manually combining equal amounts of each raw material. The validation set was pre-processed and classified using the same workflow as the calibration dataset. Class-wise and overall accuracy were also calculated for the external validation set.

Finally, the PLS-DA model was applied pixel by pixel to the hyperspectral images of the compost samples to obtain classification maps. Each hyperspectral cube was reshaped into a two-dimensional matrix of pixel spectra, pre-processed as described above, and pixels were assigned to the class with the highest predicted score (hard classification

approach). The resulting classifications were displayed as false-colour maps. Class abundance was subsequently calculated as the percentage of pixels assigned to each class relative to the total number of classified pixels in the image.

3. Results and discussion

3.1. Quantitative hyperspectral modelling of compost quality parameters

The potential of near-infrared hyperspectral imaging (NIR-HSI) for the quantitative prediction of compost quality was evaluated using PLS regression models developed from the mean spectra of the samples. This approach enables the establishment of quantitative relationships between spectral features and key physicochemical parameters relevant to compost maturation.

Four parameters were selected due to their central role in compost quality assessment [24]: loss-on-ignition (LOI), reflecting organic matter content and its transformation during composting; the carbon-to-nitrogen (C/N) ratio, a classical indicator of compost stabilisation and nitrogen availability; pH, providing information on biochemical evolution, potential phytotoxicity and nutrient dynamics; and electrical conductivity (EC), related to soluble salt content and agronomic suitability. Statistical information of reference values of both calibration and validation set is provided in P. Rueda et al. [21]. The number of LVs needed for each PLS model was selected according to the minimum RMSECV obtained during cross-validation, ensuring an adequate balance between predictive performance and model complexity. Depending on the target parameter, the models required different preprocessing strategies and numbers of LVs, explaining between 99.48 and 99.87 % of the spectral variance. Table 1 summarizes the results obtained for each parameter after optimization and plots of predicted versus measured values for all developed PLS models are provided in Fig. S2.

The prediction accuracy of the PLS model for the C/N ratio was slightly higher compared with the other parameters, achieving an RPD >3, which indicates excellent predictive performance [22]. This finding is particularly relevant since the C/N is a legislated criterion of compost maturity [25,26], making its robust prediction by NIR-HSI a significant analytical outcome. Conversely, although still displaying adequate R^2 pred values (ranging from 0.82 to 0.84), the models developed for pH, EC and LOI yielded RPD values around 2.5, consistent with good predictive performance for semi-quantitative applications. In this study, comparable and slightly superior PLS performance metrics were obtained relative to those reported by P. Rueda et al. [21] using a conventional benchtop FT-NIR spectrometer for equivalent purposes. In that work, FT-NIR measurements were performed on samples placed in a rotating sample cup, resulting in spectra averaged over the measurement area. Here, the inherently larger sampling area captured in NIR-HSI integrates spectral information over a much larger surface of the sample and therefore better reflects its intrinsic heterogeneity. Furthermore, the inclusion of samples spanning the full composting process allowed the predictive capability of NIR-HSI to be evaluated across different composting stages and conditions (see Fig. S3).

Table 1
Results and preprocessing details of PLS regression models based on near-infrared hyperspectral images (NIR-HSI) for compost quality prediction.

	Spectral pre-treatment	LVs	R^2 cal	RMSEC	R^2 pred	RMSEP	RPD
LOI (%)	Detrend + SNV	7	0.81	2.2	0.82	2.3	2.4
C/N	SNV	8	0.70	2.1	0.89	1.4	3.1
pH	2nd derivative + SNV	8	0.87	0.34	0.84	0.39	2.4
EC (dS m^{-1})	Detrend + SNV	8	0.78	0.52	0.83	0.46	2.5

LOI: organic matter expressed as “loss-on-ignition”; C/N: carbon-to-nitrogen ratio; EC: electrical conductivity; SNV: standard normal variate; LVs: latent variables; R^2 cal: determination coefficient of calibration; RMSEC: root-mean-square error of calibration; R^2 pred: determination coefficient of prediction; RMSEP: root-mean-square error of prediction; RPD: residual prediction deviation.

The Variable Importance in Projection (VIP) scores analysis yielded comprehensive insights regarding the spectral features supporting each PLS model (Fig. S4). The C/N ratio exhibited a particular distribution of VIPs >1 within the regions 1650-1800 and 2200-2400 nm, mainly associated with the C–H and CH_3/CH_2 1st harmonic and combination bands linked to lipids, polysaccharides and nitrogen-containing compounds, thus reflecting the dual role of carbon and nitrogen allocation in compost stability. In composted materials, acidity/alkalinity is largely governed by the balance between chemical species such as carboxylic acids, ammonium and carbonate ions [27]. While pH is a property measured in the aqueous extract, its prediction via NIR spectroscopy is supported by spectral features associated with these solid-phase constituents, which act as surrogate markers for the acid-base equilibrium. In particular, the VIP profile of the pH model highlights relevant contributions from vibrations attributable to O–H stretching overtones (1850-2000 nm) [28], which are associated with water and hydroxyl groups involved in acid-base equilibria. In addition, the relevance of the 2160-2300 nm region, which has been associated with carbonate-related combination bands [29], suggests that the model captures spectral information linked to carbonate content.

Regarding electrical conductivity model, the most influential spectral features were identified at shorter wavelengths with main features at 1386 and 1619 nm. Although the most of the soluble ions responsible for EC do not exhibit direct NIR absorption [30], EC can be accurately predicted through their indirect effects on the spectral features of the organic matrix, as they induce perturbations in the absorption peaks of O–H and C–H bonds of the biomass [31]. This indirect quantification relies on the ability of ionic solutes to perturb the hydrogen-bonded network of water [32] and the hydration shells of water adsorbed onto compost constituents, such as cellulose. Additionally, certain salts carry water of crystallization that remains stable after the drying process (65 °C), contributing specific vibrational signatures [33]. These alterations in the water's state combined with the shifts in the organic functional groups' bands, enable the PLS model to correlate spectral variance with the ionic content measured in the reference extracts. While fluctuations in residual moisture could affect NIR predictions, the robustness of the external validation confirms that these effects do not compromise the accuracy of the model in providing a reliable proxy for EC.

LOI predictions were influenced by broader features extending over the range 1140-2000 nm, including lipid, protein, water and carbohydrate bands, in line with what would be expected when considering the total organic matter content [34]. The comprehensive analysis of the VIP profiles reveals partial overlap across models but also distinct parameter-specific spectral domains consistent with their chemical basis, thereby increasing confidence in the robustness of the calibrated models. For properties such as pH and EC, where complex molecular interactions at both micro and macro scales correlate with the target property, the spectral interpretation can be challenging. Nevertheless, the representativeness of the sample set ensures that these correlations are consistent and reliable. Consequently, the models are supported by empirical validation, confirming their ability to capture the chemical variability during the composting process within the established experimental margins.

Unlike benchtop NIR instruments, hyperspectral imaging provides not only average information/parameters’ estimations at the sample-level but also detailed information regarding their spatial distribution, thereby highlighting compositional heterogeneity that would otherwise remain unnoticed. Thus, the optimized PLS models were subsequently applied on a pixel-wise basis to generate spatially resolved prediction maps, enabling direct visualization of compost dynamics at different

stages (Fig. 1).

Fig. 1c and d illustrate the LOI and C/N maps as representative examples, while similar spatial and temporal patterns were observed for pH and EC. The decrease in LOI, the gradual reduction of the C/N ratio, and the changes of pH and EC can all be monitored both as overall averages and through their spatial distribution across the compost sample, providing additional nuance. Beyond assessing spatial uniformity, the prediction maps provided deeper insight into temporal trends in key parameters relevant for effective compost maturity monitoring. In general, a progressive reduction in variability and a convergence of pixel values toward more uniform distributions were observed in the PLS prediction maps as composting time increased, which can be interpreted as a sign of compost maturation. However, given the complexity of the material, longer composting times do not always guarantee a better-quality end product, as residual heterogeneity and partially decomposed raw materials may persist and affect quality parameters when time is considered in isolation.

Accordingly, these maps further revealed specific regions where values remained suboptimal despite prolonged composting, underscoring the inherent variability of industrial-scale processes, wherein aeration, moisture distribution, and mixing efficiency can lead to uneven decomposition. Identifying such suboptimal zones enables targeted corrective actions, such as localized turning, moisture adjustment, or process optimisation, rather than uniform interventions across the entire pile.

Although PLS-based prediction provides a robust and highly informative framework for linking spectral data with key physicochemical parameters, these parameters alone do not fully describe the overall compositional evolution of composting materials. In practice, only a limited number of laboratory reference measurements can be routinely acquired, while additional composition-related factors also contribute to compost quality.

While pixel-wise PLS prediction maps reveal local spatial and temporal variations in these key parameters, the broader dynamics of composting are also strongly driven by changes in the relative contribution, distribution and transformation of the different compositional fractions. In this context, complementary multivariate strategies based on spectral information enable a more direct interpretation of compositional transitions without requiring additional laboratory-based reference measurements. Together, quantitative PLS prediction and spectral-based classification approaches provide a more comprehensive and practical framework for composting process monitoring.

3.2. Pixel-wise composting assessment by PLS-DA

To further investigate the compositional evolution occurring during the composting process beyond classical physicochemical parameters, a supervised classification approach based on partial least squares discriminant analysis (PLS-DA) was applied to the hyperspectral data. In contrast to the quantitative regression models, this approach focuses on identifying spectral patterns associated with the relative contribution and transformation of the different raw materials throughout composting. Rather than a strict classification, this strategy serves as a tool to track the compositional evolution of the material by treating the initial raw materials and the stabilized end-product as boundary classes.

The main physicochemical characteristics of the five classes considered in the PLS-DA model are summarized in Table S1. The raw olive-derived biomasses (OMP and OTP) exhibited high organic matter contents (LOI: 91.9 % and 84.7 %, respectively) and elevated C/N ratios (32 %–37 %), consistent with its lignocellulosic nature. In contrast, animal manures (CM and GM) were characterized by high nitrogen levels (up to 3.3 % in CM) and lower C/N ratios. Furthermore, animal manures exhibited alkaline pH and higher values of EC than plant-based raw materials(OMP and OTP). The mature compost (COMP) displayed the physicochemical characteristics typically associated with significant organic matter mineralization (LOI decreased to 64.3 %). Furthermore, composting induced a marked pH increase to alkaline levels and stabilized the C/N ratio at 15.7, a value lower than the original biomasses but higher than the values typical of animal manures. These compositional differences are also reflected in their spectral features. Fig. 2 shows the average spectra of the five considered classes: olive mill pomace, olive tree pruning, goat and chicken manures, and the 33-week compost (COMP). All of them exhibited broadly similar shapes, as would be expected for organic matrices. However, noticeable intensity differences were observed in the regions around 1400-1900 nm and 2000-2400 nm, mainly related to O–H, N–H, and C–H absorptions [34].

These spectral variations are indicative of intrinsic compositional differences among the raw materials and the more advanced degree of organic matter transformation in COMP, indicating that spectral discrimination among classes should be feasible. This was further supported by an exploratory PCA performed on the 20000 pixel spectra used for PLS-DA calibration (Fig. 3) where the score plots revealed class-dependent distributions within the multivariate space. Specifically, PC1, accounting for 84.38 % of the total variance, separates the composted material (COMP) from the raw feedstocks, despite some overlap due to the compositional similarities inherent to organic materials. Regarding the feedstocks, OMP and OTP exhibited the broadest score distributions, spanning almost the area defined by PC1 and PC2. Interestingly, a subset of pixels from GM and CM was projected towards the positive area of PC2, together with OMP and OTP pixel scores, likely reflecting the presence of plant-based bedding materials in their composition, which may contribute spectral features similar to those of lignocellulosic materials. Furthermore, in the space defined by PC1 and PC3, these olive-derived feedstocks (OMP and OTP) partially overlapped with each other while differentiating from the manure-based feedstocks (GM and CM) and final compost.

The PLS-DA model was developed at the pixel level with independent samples from each pure class, and was subsequently validated through internal cross-validation and external testing on both new individual materials and mixtures. The PLS-DA model retained 8 LVs, providing an optimal balance between classification accuracy and model complexity. Under these conditions, the model enabled a robust discrimination between the target classes, focusing on chemically meaningful spectral differences rather than physical variability. The resulting classification performance is summarised in Table 2.

The PLS-DA model showed robust and consistent performance across calibration, cross-validation, and external validation. All internal metrics exceeded 0.93, with the majority above 0.97. OMP and CM showed the highest F1-score values (>0.98), while OTP, GM and COMP exhibited slightly lower performance. It is worth noting that extracting calibration pixels from a single representative image per class may introduce spatial autocorrelation and risk pseudo-replication. Nevertheless, the external validation, with F1-scores ranging from 0.95 to 0.99 and an overall accuracy of 94.0 %, demonstrates that the model is not overfitted and possesses genuine predictive power. Because the external validation set consisted of independent samples, these results demonstrate that the model captured genuine chemical differences, confirming its generalization capability across heterogeneous materials.

Analysis of the confusion matrix (Table S1) revealed that misclassifications were systematic and closely related to chemical and structural similarities among classes. OMP and CM showed the highest classification accuracies, with correct classification rates above 90 % in the external validation dataset, indicating the presence of distinctive NIR spectral signatures. In contrast, OTP, GM, and COMP exhibited higher levels of mutual confusion. Approximately 10 % of GM pixels were misclassified as OMP, reflecting similarities in organic matter composition and moisture-related spectral features. Likewise, OTP showed relevant confusion with COMP ($\sim$ 3 %), consistent with their shared lignocellulosic nature, while COMP displayed misclassification rates of about 4 % towards OMP and 3 % towards OTP, supporting its role as an intermediate material integrating spectral characteristics of the different feedstocks. Such confusion patterns were already suggested

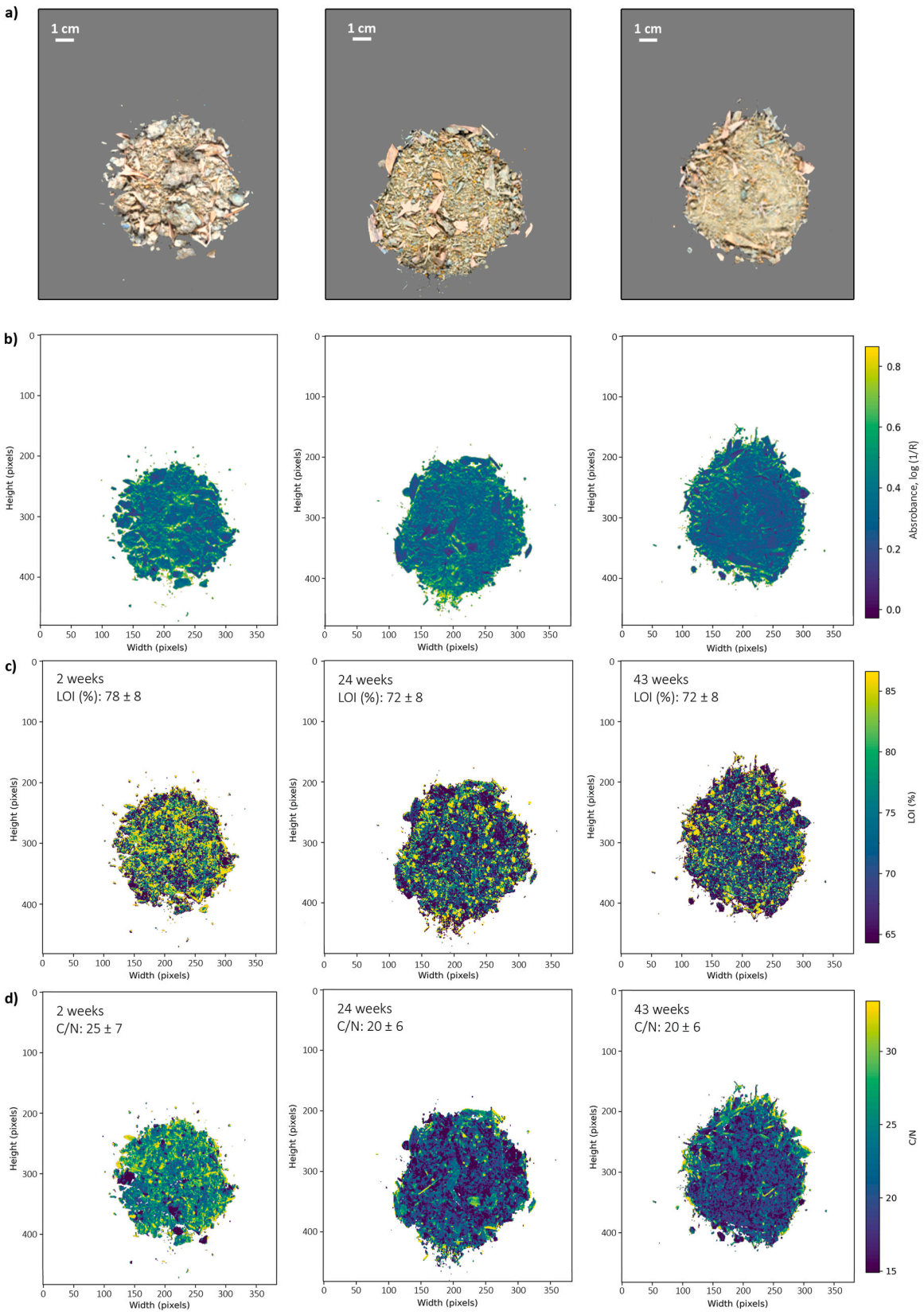

Fig. 1. (a) RGB images of representative compost samples. (b) Corresponding near-infrared hyperspectral images of the same samples after background removal, with the colour scale representing average absorbance values expressed as log(1/R). (c–d) Examples of pixel-wise prediction maps obtained using the optimised PLS regression models for compost quality parameters: (c) loss-on-ignition (LOI) and (d) carbon-to-nitrogen (C/N) ratio, shown for samples collected at 2, 24 and 43 weeks of composting from sampling sector 3 of the 2020/2021 campaign. Colour bars indicate the predicted values of each parameter. (For interpretation of the references to colour in this figure legend, the reader is referred to the Web version of this article.)

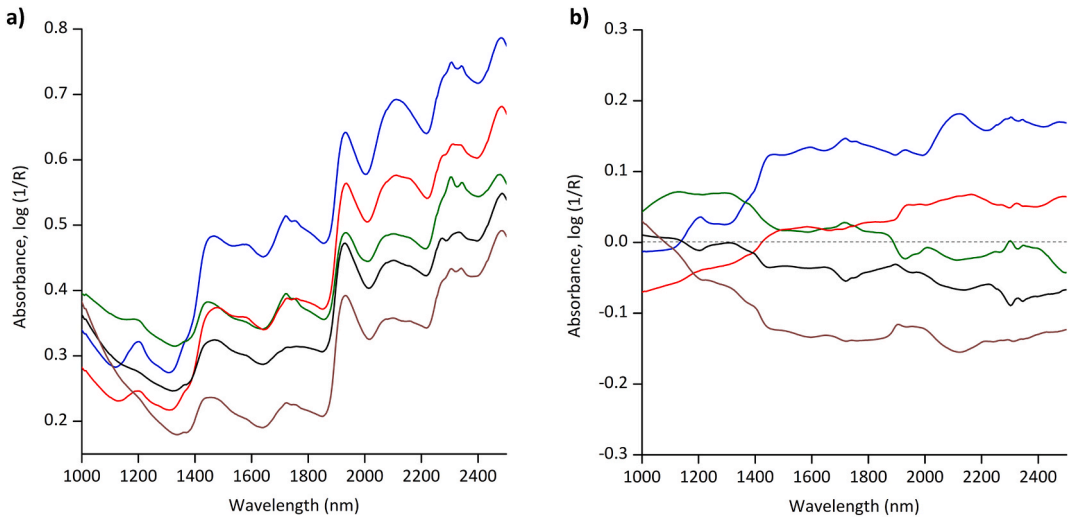

Fig. 2. a) Mean NIR-HSI spectra of the five classes considered in the PLS-DA model; b) difference between class-averaged spectra and the overall mean spectrum. Colour code: ■ olive mill pomace (OMP); ■ olive tree pruning (OTP); ■ goat manure with straw bedding (GM); ■ chicken manure with sawdust bedding (CM); ■ 33-week composted olive mill pomace (COMP). (For interpretation of the references to colour in this figure legend, the reader is referred to the Web version of this article.)

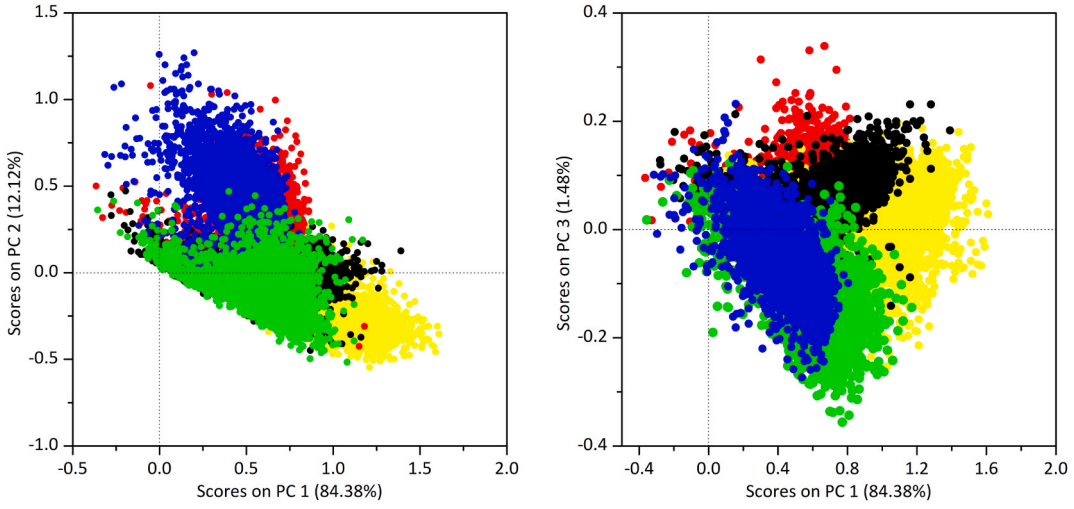

Fig. 3. PCA score plots (PC2 vs. PC1 and PC3 vs. PC1) obtained from the 20000 pixel spectra used for PLS-DA calibration (4000 pixel each class). Colour code: ● olive mill pomace (OMP); ● olive tree pruning (OTP); ● goat manure with straw bedding (GM); ● chicken manure with sawdust bedding (CM); ● 33-week composted olive mill pomace (COMP). (For interpretation of the references to colour in this figure legend, the reader is referred to the Web version of this article.)

Table 2
Performance metrics of PLS-DA model for calibration, cross-validation and external validation.

Class	Calibration			Cross validation			External validation			
	Sens	Spec	F1-score	Sens	Spec	F1-score	Sens	Spec	F1-score	Acc (%)
OMP	0.992	0.997	0.990	0.992	0.997	0.990	0.988	0.997	0.991	98.1
OTP	0.937	0.991	0.950	0.936	0.991	0.950	0.928	0.997	0.959	94.3
GM	0.951	0.983	0.941	0.948	0.983	0.940	0.958	0.995	0.969	87.6
CM	0.988	0.994	0.983	0.988	0.994	0.982	0.989	0.992	0.985	98.1
COMP	0.930	0.984	0.933	0.930	0.983	0.931	0.985	0.983	0.981	91.9

OMP: olive mill pomace; OTP: olive tree pruning; GM: goat manure with straw bedding; CM: chicken manure with sawdust bedding; COMP: 33-week composted olive mill pomace; Sens: sensitivity; Spec: specificity; Acc: accuracy.

by the partial overlap observed in the PCA score plots and point to the existence of shared spectral features among the different defined classes.

The VIP profiles (Fig. 4) provided further insight into the spectral regions responsible for the observed class similarities and misclassifications. The region between 2100 and 2300 nm showed the strongest influence, dominated by lignocellulosic absorptions [35] that appeared most prominently in OTP but were also characteristic of GM and CM due to the presence of straw- and sawdust-based bedding. Based

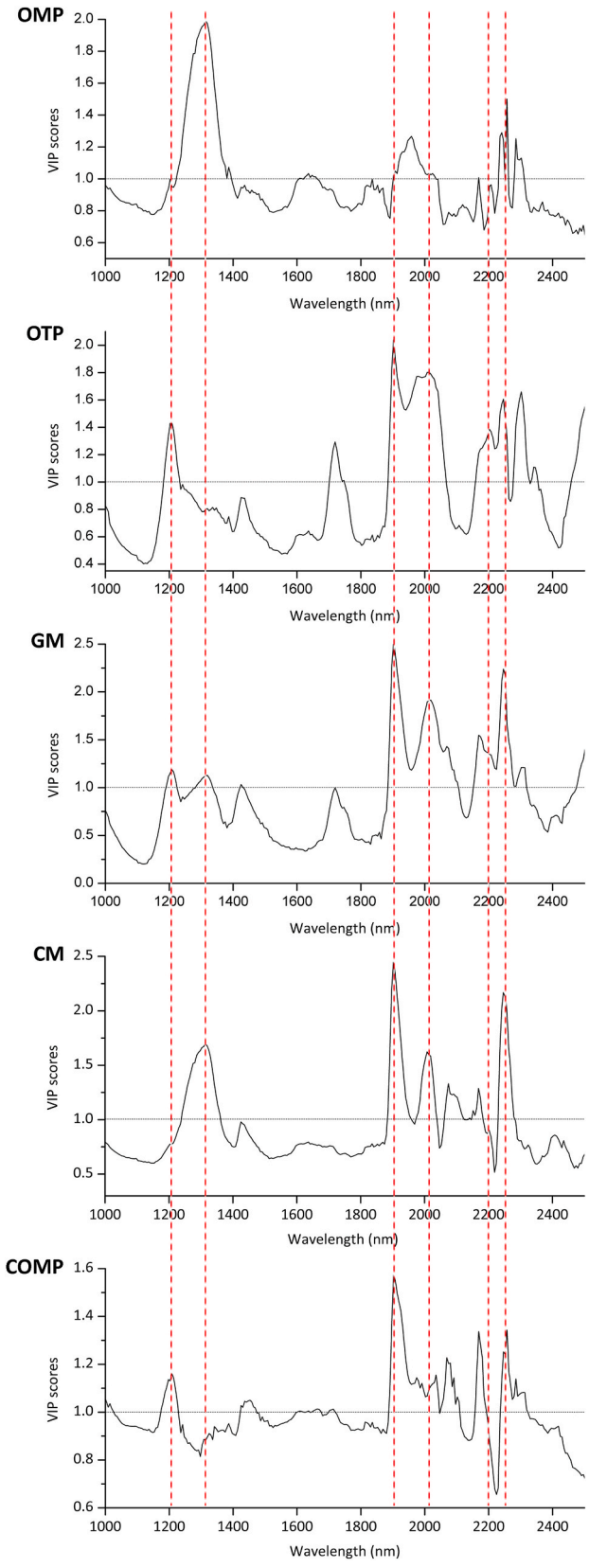

Fig. 4. VIP scores of the PLS-DA model per class. Major discriminant spectral bands are indicated by red grid lines. OMP: olive mill pomace; OTP: olive tree pruning; GM: goat manure with straw bedding; CM: chicken manure with sawdust bedding; COMP: 33-week composted olive mill pomace. (For interpretation of the references to colour in this figure legend, the reader is referred to the Web version of this article.)

on the existing literature, bands at wavelengths close to 2100 nm are associated with combination bands involving O–H and C–H stretching vibrations in hemicellulose, cellulose and lignin, whereas those around 2300 nm are mainly attributed to the C–H stretching and deformation vibrations in these compounds [36]. The presence of lignocellulosic features in OTP, GM and CM leads to the convergence of such classes within the classification.

Additional ambiguity arose from the 1900–2200 nm region, characterized by strong O–H combination bands and overlapping absorptions related to nitrogen-containing organic compounds [37]. These nitrogen-related features are notably pronounced in manure-derived materials and thus strongly expressed in GM and CM. Although OTP also exhibited spectral contributions in this region, their weaker and less defined signature, also partially masked by the more dominant lignocellulosic absorptions at longer wavelengths, suggested a reduced nitrogen contribution.

At lower wavelengths, spectral features around 1250 nm also contributed to class discrimination. These bands were especially prominent in OMP and are associated with C–H and CH_2 overtone vibrations from aliphatic chains, as well as to O–H overtones from lignocellulosic materials and phenolic moieties [28,38,39]. The stronger intensity of these bands in OMP is consistent with its higher lipid content and aligns with the high sensitivity and F1-score values reported for this class.

The final stage compost class showed comparatively lower classification performance metrics, likely reflecting its greater compositional heterogeneity and higher spectral variability. Its main VIP contributions overlapped with those of manure-derived materials, including nitrogen-associated absorptions and residual lignin-derived bands. Additional contributions observed between 1900 and 2100 nm probably reflect absorptions associated with aromatic and humic-like structures that progressively accumulate during composting [40]. The persistence of these recalcitrant fractions explains the frequent misclassification of COMP towards GM and CM, with occasional confusion with OTP, and further supports the relevance of nitrogen-rich signals as spectral markers of compost stabilisation.

Once validated, the PLS-DA model was applied to the hyperspectral images of the compost samples collected throughout the process. Fig. 5 presents some examples of hyperspectral image analysis at different composting stages in the form of false-colour maps, showing the distribution of the different classes within the samples. Comparisons across composting times reveal a notable temporal evolution in the relative abundance of the different components.

At the early stage (<5 composting weeks), the mixture was dominated by non-decomposed raw materials, comprising 57 % OMP, 25 % OTP, and 6 % animal manure. It should be noted that the OTP fraction may also include pixels associated with other plant-derived residues, such as manure bedding. The remaining pixels (12 %) were classified as COMP, reflecting localized areas with spectral features similar to those of mature compost. However, this classification most likely reflects spectral resemblance rather than actual compost formation at this stage. This behaviour is consistent with the overlap observed in the VIP profiles, particularly in key spectral regions associated with lignocellulosic structures and nitrogen-containing compounds, which are already present in the raw materials.

As composting proceeded, the feedstock materials became less dominant and appeared in more fragmented clusters, while regions classified as COMP increased noticeably (∼ 45 %). This finding suggests that a significant proportion of the mixture had already undergone structural and biochemical transformation, although residual signatures of the initial components were still detectable across the material. In the more advanced sample (>32 composting weeks), most of the pixels (87 %) are attributed to the COMP class, reflecting the compositional evolution of the material during composting and its gradual convergence towards a more homogeneous state. This behaviour is consistent with literature indicating that composting aims to produce a stable, uniform material through progressive decomposition of raw materials [41].

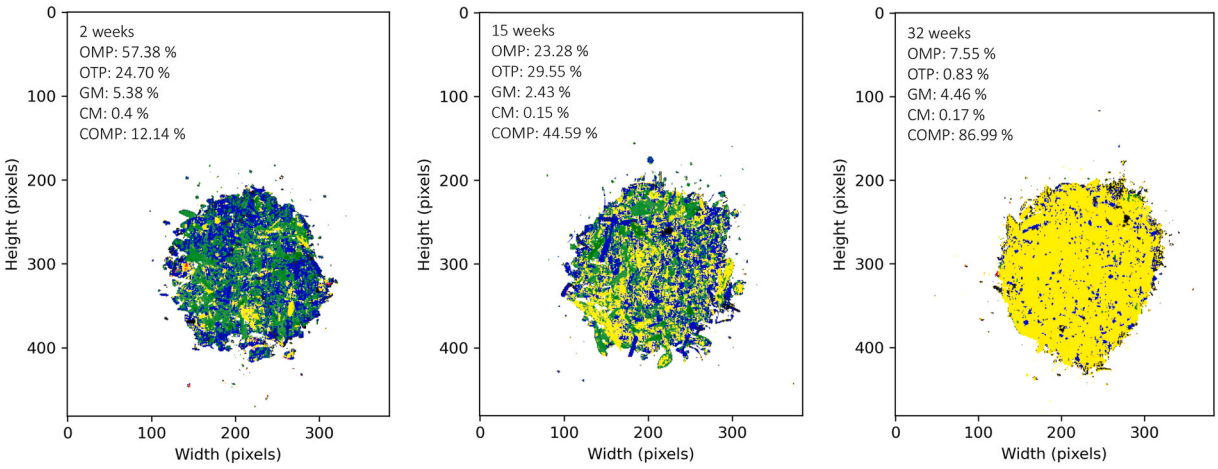

Fig. 5. Example of pixel-wise PLS-DA classification maps for early (2 weeks), intermediate (15 weeks) and advanced (32 weeks) compost samples, showing the most probable class assigned to each pixel: ■ olive mill pomace (OMP); ■ olive tree pruning (OTP); ■ goat manure with straw bedding (GM); ■ chicken manure with sawdust bedding (CM); ■ 33-week composted olive mill pomace (COMP).

It should be noted that the PLS-DA model always forces each pixel to be assigned to one of the predefined classes even for intermediate states with degraded materials that do not perfectly match the initial inputs or the final compost. Since each pixel was assigned to the class yielding the highest predicted score, pixel counts can be interpreted as a relative measure of the prevalence of spectral characteristics associated with each class. Applying this pixel-counting approach to all samples enabled the construction of evolution curves (Fig. 6), providing a temporal view

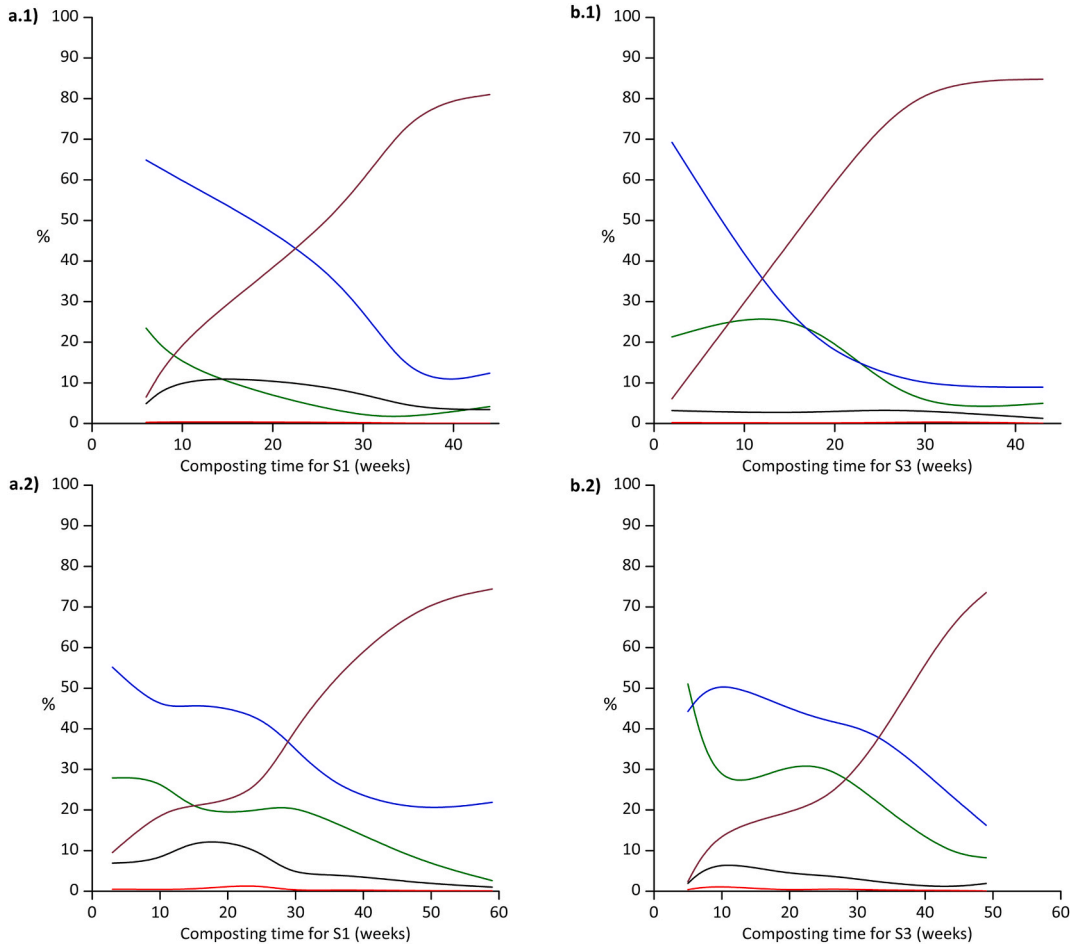

Fig. 6. Temporal evolution of the percentage of pixels assigned to each PLS-DA class throughout the composting process for sampling sectors 1 (a) and 3 (b) of the 2020/2021 (1) and 2021/2022 (2) olive harvest campaigns. Colour code: ■ olive mill pomace (OMP); ■ olive tree pruning (OTP); ■ goat manure with straw bedding (GM); ■ chicken manure with sawdust bedding (CM); ■ 33-week composted olive mill pomace (COMP). (For interpretation of the references to colour in this figure legend, the reader is referred to the Web version of this article.)

of the evolution of these spectral signatures throughout composting. The numerical values underlying these curves are provided in Table S3. As composting progressed, the proportion of pixels showing greater similarity to the initial raw materials decreased in favour of those associated with the COMP class, providing a semiquantitative indicator of compost maturation.

In the 2020/2021 season, this shift was rapid and uniform, with a consistent reduction of raw-material pixels and an early consolidation of the COMP class, whereas the 2021/2022 campaign showed a more gradual progression with OMP and OTP pixels persisting for longer periods. These pixel-based PLS-DA trends are coherent with the evolution of conventional maturity indicators (see Fig. S3a and S3b). The 2020/2021 campaign exhibited a steady decrease in the C/N ratio, reflecting enhanced mineralisation and stabilisation, while 2021/2022 showed a less uniform C/N evolution with time. Operational factors likely contributed to these differences: limited turning in early stages may have restricted oxygen availability, and elevated pH values observed in the final stages of 2021/2022 (over 9.0) could have inhibited microbial activity and delayed stabilisation.

The variability across sectors within each campaign can be attributed to the operational management strategies employed during the construction of the pile and subsequent turning times. Although the entire pile is turned on the same dates, systematic aeration does not begin until the pile is complete, so each sector experiences different conditions beforehand. Faster stabilisation was observed in those sectors subjected to earlier overturning, as reflected in the pixel dynamics with sector 3 (20/21) showing a particularly clear and earlier stabilization of the COMP class. Frequent or earlier turnings can lead to the acceleration of the decomposition of organic matter along with an increase in microbial activity [42,43].

Differences between campaigns can be attributed to a combination of environmental and operational factors. Seasonal weather conditions, particularly temperature and rainfall, may have directly influenced the moisture content of the pile and oxygen availability, which are critical for microbial activity [44]. In particular, the 2020/2021 campaign was characterised by lower and more irregular precipitation together with a gradual decrease in ambient temperature during the sampling period, whereas the 2021/2022 campaign experienced more frequent rainfall events and higher cumulative precipitation, especially at earlier stages. These conditions together with differences in the composition and physicochemical properties of the feedstock mixture could have contributed to the lower degradation rates observed throughout the latter campaign.

The conversion of classification maps into compositional metrics represents a novel analytical application of NIR-HSI combined with pixel-based PLS-DA. This approach enables the monitoring of relative abundance of raw materials and mature compost at each stage. It should be noted that, beyond the initial composting stages, these proportions do not represent the actual concentration of the original feedstocks but rather the prevalence of their molecular signatures as decomposition progresses and material identity is lost. In this sense, pixel class assignments must be interpreted as a spectral representation of prevailing chemical signatures rather than as a direct measure of the physical presence of the original feedstocks. This quantitative framework allows the definition of maturation thresholds that are based on the residual content of raw materials, hence reinforcing the efficacy as a reliable control tool. Furthermore, any deviation from the expected behaviour can be interpreted as an early warning indicator of excessive heterogeneity or suboptimal process performance, as can be seen in the example of the campaign 2021/2022. This approach is readily transferable to other bioprocesses and industrial systems that require temporal monitoring of input material transformation.

4. Conclusions

NIR hyperspectral imaging combined with multivariate modelling was applied for the first time as a promising framework for monitoring an industrial olive mill pomace composting process. PLS regression models developed for key physicochemical maturity parameters achieved better predictive performance compared with conventional point-based NIR measurements (RPD >2.5). This improvement is mainly attributed to the greater spatial representativeness provided by hyperspectral imaging, which captures material heterogeneity and reduces sampling bias, while enabling spatially resolved monitoring of compost quality throughout the process.

In addition, pixel-wise PLS-DA classification enabled the assessment of compositional evolution from raw materials to stabilised compost through the analysis of dominant spectral signatures. Although class proportions reflect spectral similarity rather than the actual physical abundance of individual feedstocks, this approach revealed spatial heterogeneity, sector-specific behaviours and localised delays in organic matter degradation that would likely remain undetected using conventional methodologies. While the current validation results confirm the reliability of these findings, future calibration strategies should incorporate smaller, independent sub-images from multiple material batches to better capture natural variability. Overall, the proposed strategy provides operationally relevant information for *in situ* process monitoring and optimisation, with possible application to other heterogeneous bioprocesses, such as anaerobic digestion.

CRediT authorship contribution statement

Marta P. Rueda: Data curation, Formal analysis, Investigation, Methodology, Software, Writing – original draft, Writing – review & editing. **Antoine Deryck:** Data curation, Investigation, Methodology, Software, Writing – review & editing. **François Stevens:** Data curation, Investigation, Methodology, Software, Writing – review & editing. **Juan Antonio Fernández Pierna:** Conceptualization, Investigation, Methodology, Software, Supervision, Writing – review & editing. **Vincent Baeten:** Investigation, Methodology, Supervision, Writing – review & editing. **María José Ayora-Cañada:** Conceptualization, Funding acquisition, Investigation, Project administration, Resources, Supervision, Validation, Writing – original draft, Writing – review & editing. **Ana Domínguez-Vidal:** Conceptualization, Investigation, Supervision, Validation, Writing – original draft, Writing – review & editing.

Declaration of competing interest

The authors declare that they have no known competing financial interests or personal relationships that could have appeared to influence the work reported in this paper.

Acknowledgements

This work has been financed by the research project PID2020-118673RB-I00 by MCIN/AEI/10.13039/501100011033 (Spanish Ministry of Science and Innovation). The authors thank Nicaise Kayoka Mukendi, technical staff member at CRA-W, for his technical assistance during the NIR-HSI measurements. Marta P. Rueda also acknowledges the FPU22/00016 fellowship from the Spanish Ministry of Universities. Funding for open access charge: Universidad de Jaén/CBUA.

Appendix A. Supplementary data

Supplementary data to this article can be found online at https://doi.org/10.1016/j.talanta.2026.130201.

Data availability

Data will be made available on request.

References

[1] L. Becker, J. Sturm, F. Eiden, D. Holtmann, Analyzing and understanding the robustness of bioprocesses, Trends Biotechnol. 41 (2023) 1013–1026, https://doi.org/10.1016/j.tibtech.2023.03.002.

[2] Y. Yang, Y. Kong, G. Wang, Y. Shen, R. Tang, Z. Yin, J. Yang, G. Li, J. Yuan, Temporal succession and spatial heterogeneity of humification, pathogens and bacterial community in facultative heap composting, Process Saf. Environ. Prot. 176 (2023) 734–746, https://doi.org/10.1016/j.psep.2023.06.049.

[3] S. Pinzi, F. Alonso, J. García Olmo, M.P. Dorado, Near infrared reflectance spectroscopy and multivariate analysis to monitor reaction products during biodiesel production, Fuel 92 (2012) 354–359, https://doi.org/10.1016/j.fuel.2011.07.006.

[4] Y.Z. Feng, G. Elmasry, D.W. Sun, A.G.M. Scannell, D. Walsh, N. Morcy, Near-infrared hyperspectral imaging and partial least squares regression for rapid and reagentless determination of enterobacteriaceae on chicken fillets, Food Chem. 138 (2013) 1829–1836, https://doi.org/10.1016/j.foodchem.2012.11.040.

[5] J.A. Fernández Pierna, P. Vermeulen, D. Eylenbosch, J. Burger, B. Bodson, P. Dardenne, V. Baeten, Chemometrics in NIR hyperspectral imaging: theory and applications in the agricultural crops and products sector, in: Compr. Chemom., second ed., 2020, pp. 361–379, https://doi.org/10.1016/B978-0-12-409547-2.14811-5.

[6] M.F. Cheng, A. Mukundan, R. Karmakar, M.A.E. Valappil, J. Jouhar, H.C. Wang, Modern trends and recent applications of hyperspectral imaging: a review, Technol. 13 (2025) 170, https://doi.org/10.3390/technologies13050170.

[7] M. Jiang, Y. Li, J. Song, Z. Wang, L. Zhang, L. Song, B. Bai, K. Tu, W. Lan, L. Pan, Study on black spot disease detection and pathogenic process visualization on winter jujubes using hyperspectral imaging system, Foods 12 (2023) 435, https://doi.org/10.3390/foods12030435.

[8] M.A.E. Abdelrahman, M.M. Metwaly, T.M.H. Yossif, A.R.A. Moursy, Using hyperspectral data to estimate and map surface and subsurface soil salinity, pH, and calcium carbonates in arid region, Environ. Sustain. 8 (2025) 367–387, https://doi.org/10.1007/S42398-025-00355-X.

[9] D. Malavi, A. Nikkhah, P. Alighaleh, S. Einafshar, K. Raes, S. Van Haute, Detection of saffron adulteration with crocus sativus style using NIR-hyperspectral imaging and chemometrics, Food Control 157 (2024) 110189, https://doi.org/10.1016/j.foodcont.2023.110189.

[10] J.P. Cruz-Tirado, J.A. Fernández Pierna, H. Rogez, D.F. Barbin, V. Baeten, Authentication of cocoa (Theobroma cacao) bean hybrids by NIR-hyperspectral imaging and chemometrics, Food Control 118 (2020) 107445, https://doi.org/10.1016/j.foodcont.2020.107445.

[11] J.A. Fernández Pierna, V. Baeten, A.M. Renier, R.P. Cogdill, P. Dardenne, Combination of support vector machines (SVM) and near-infrared (NIR) imaging spectroscopy for the detection of meat and bone meal (MBM) in compound feeds, J. Chemom. 18 (2004) 341–349, https://doi.org/10.1002/cem.877.

[12] L. Xie, R. Wang, J. Tian, S. Yu, X. Wan, H. Yang, X. Hu, M. Chen, H. Zhang, J. Yang, Y. Peng, S. Liu, Hyperspectral imaging for monitoring quality changes in Nongxiang Baijiu Daqu fermentation, Microchem. J. 217 (2025) 114973, https://doi.org/10.1016/j.microc.2025.114973.

[13] S. Jin, X. Liu, J. Wang, L. Pan, Y. Zhang, G. Zhou, C. Tang, Hyperspectral imaging combined with fluorescence for the prediction of microbial growth in chicken breasts under different packaging conditions, LWT 181 (2023) 114727, https://doi.org/10.1016/J.LWT.2023.114727.

[14] C.S.S. Ferreira, S. Seifollahi-Aghmiuni, G. Destouni, N. Ghajarnia, Z. Kalantari, Soil degradation in the European mediterranean region: processes, status and consequences, Sci. Total Environ. 805 (2022) 150106, https://doi.org/10.1016/j.scitotenv.2021.150106.

[15] United States Composting Council, Test Methods for the Examination of Composting and Compost, 2015.

[16] D.W. Nelson, L.E. Sommers, Total carbon, organic carbon, and organic matter, in: A.L. Page, R.H. Miller, D.R. Kenney (Eds.), Methods of Soil Analysis: Part 2 Chemical and Microbiological Properties, Agronomy Monographs, 1982, pp. 539–579, https://doi.org/10.2134/agronmonogr9.2.2ed.c29.

[17] K.P. Sinaga, Y. Miin-Shen, Unsupervised K-means clustering algorithm, IEEE Access 8 (2020) 80716–80727, https://doi.org/10.1109/access.2020.2988796.

[18] A. Savitzky, M.J.E. Golay, Smoothing and differentiation of data by simplified least squares procedures, Anal. Chem. 36 (2002) 1627–1639, https://doi.org/10.1021/ac60214a047.

[19] O. Meinander, W. Josefsson, J. Kaurola, T. Koskela, K. Lakkala, Spike detection and correction in brewer spectroradiometer ultraviolet spectra, Opt. Eng. 42 (2003) 1812–1819, https://doi.org/10.1117/1.1569492.

[20] O. Alghushairy, R. Alsini, T. Soule, X. Ma, A review of local outlier factor algorithms for outlier detection in big data streams, Big Data Cogn. Comput. 5 (2020) 1–24, https://doi.org/10.3390/bdcc5010001.

[21] M.P. Rueda, A. Domínguez-Vidal, V. Aranda, M.J. Ayora-Cañada, Monitoring the composting process of olive oil industry waste: Benchtop FT-NIR vs. miniaturized NIR spectrometer, Agronomy 14 (2024) 3061, https://doi.org/10.3390/agronomy14123061.

[22] W. Saeys, A.M. Mouazen, H. Ramon, Potential for onsite and online analysis of pig manure using visible and near infrared Reflectance Spectroscopy, Biosyst. Eng. 91 (2005) 393–402, https://doi.org/10.1016/j.biosystemseng.2005.05.001.

[23] B. Mahieu, E.M. Qannari, B. Jaillais, Extension and significance testing of Variable Importance in Projection (VIP) indices in partial Least squares regression and principal components analysis, Chemom. Intell. Lab. Syst. 242 (2023) 104986, https://doi.org/10.1016/j.chemolab.2023.104986.

[24] K. Azim, B. Soudi, S. Boukhari, C. Perissol, S. Roussos, I. Thami Alami, Composting parameters and compost quality: a literature review, org, Agric. 8 (2017) 141–158, https://doi.org/10.1007/S13165-017-0180-Z.

[25] BOE, Real Decreto 999/2017, de 24 de noviembre, por el que se modifica el Real Decreto 506/2013, de 28 de junio, sobre productos fertilizantes, Boletín Oficial Del Estado 296 (2017) 119396–119450.

[26] European Parliament and of the Council, Regulation (EU) 2019/1009 of the European Parliament and of the Council of 5 June 2019 Laying down Rules on the Making Available on the Market of EU Fertilising Products and Amending Regulations (EC) No 1069/2009 and (EC) No 1107/2009 and Repealing Regulation (EC) No 2003/2003, 2019.

[27] I. Bertrand, O. Delfosse, B. Mary, Carbon and nitrogen mineralization in acidic, limed and calcareous agricultural soils: apparent and actual effects, Soil Biol. Biochem. 39 (2007) 276–288, https://doi.org/10.1016/j.soilbio.2006.07.016.

[28] J. Workman, L. Weyer, Practical Guide and Spectral Atlas for Interpretive near-infrared Spectroscopy, second ed., CRC Press, 2012.

[29] R.N. Clark, T.V.V. King, M. Klejwa, G.A. Swayze, N. Vergo, High spectral resolution reflectance spectroscopy of minerals, J. Geophys. Res. 95 (1990) 12653–12680, https://doi.org/10.1029/JB095IB08P12653.

[30] G.D. Vyavahare, J.J. Yun, J.H. Park, J.H. Shim, S.H. Kim, K. Kim, A. Roh, H.J. Jang, S. Jeon, Evaluating the performance of NIR spectroscopy in predicting soil properties: a comparative study, Appl. Sci. 15 (2025), https://doi.org/10.3390/app152413240.

[31] R. Wu, J. Xue, H. Tian, H. Gao, Q. Zhao, C. Dong, The feasibility of detection of trace elements in corn stover based on their interference effect on the near-infrared peak of water, Spectrochim. Acta A Mol. Biomol. Spectrosc. 340 (2025) 126307, https://doi.org/10.1016/j.saa.2025.126307.

[32] A.A. Gowen, F. Marini, Y. Tsuchisaka, S. De Luca, M. Bevilacqua, C. O'Donnell, G. Downey, R. Tsenkova, On the feasibility of near infrared spectroscopy to detect contaminants in water using single salt solutions as model systems, Talanta 131 (2015) 609–618, https://doi.org/10.1016/j.talanta.2014.08.049.

[33] S. Wu, C. Wang, Y. Liu, Y. Li, J. Liu, A. Xu, K. Pan, Y. Li, X. Pan, Mapping the salt content in soil profiles using Vis-NIR hyperspectral imaging, Soil Sci. Soc. Am. J. 82 (2018) 1259–1269, https://doi.org/10.2136/SSSAJ2018.02.0074.

[34] K. Kawamura, Y. Tsujimoto, T. Nishigaki, A. Andriamananjara, M. Rabenarivo, H. Asai, T. Rakotoson, T. Razafimbelo, Laboratory visible and near-infrared spectroscopy with genetic Algorithm-based partial least squares regression for assessing the soil phosphorus content of upland and lowland rice fields in Madagascar, Remote Sens. 11 (2019) 506, https://doi.org/10.3390/rs11050506.

[35] X. Jin, X. Chen, C. Shi, M. Li, Y. Guan, C.Y. Yu, T. Yamada, E.J. Sacks, J. Peng, Determination of hemicellulose, cellulose and lignin content using visible and near infrared spectroscopy in Miscanthus sinensis, Bioresour. Technol. 241 (2017) 603–609, https://doi.org/10.1016/j.biortech.2017.05.047.

[36] X. Li, C. Sun, B. Zhou, Y. He, Determination of hemicellulose, cellulose and lignin in Moso bamboo by near Infrared spectroscopy, Sci. Rep. 5 (2015) 17210, https://doi.org/10.1038/srep17210.

[37] I. Tahmasbian, N.K. Morgan, S.H. Bai, M.W. Dunlop, A.F. Moss, Comparison of hyperspectral imaging and near-infrared spectroscopy to determine nitrogen and carbon concentrations in wheat, Remote Sens. 13 (2021) 1128, https://doi.org/10.3390/rs13061128.

[38] M.R.M. Izawa, D.M. Applin, L. Norman, E.A. Cloutis, Reflectance spectroscopy (350–2500 nm) of solid-state polycyclic aromatic hydrocarbons (PAHs), Icarus 237 (2014) 159–181, https://doi.org/10.1016/J.ICARUS.2014.04.033.

[39] M. Barea-Sepúlveda, J.L.P. Calle, M. Ferreiro-González, M. Palma, Rapid classification of petroleum waxes: a Vis-NIR spectroscopy and machine learning approach, Foods 12 (2023) 3362, https://doi.org/10.3390/foods12183362.

[40] Z. Zhang, M. Yang, A. Biswas, Spectral predictability of soil organic matter depends on its humin fraction rather than spectral fusion, Sensors 25 (2025) 7616, https://doi.org/10.3390/s25247616.

[41] D. Chimanbhai Saypariya, D. Singh, A. Kumar Dikshit, M.B. Dangi, Composting of organic fraction of municipal solid waste in a three-stage biodegradable composter, Heliyon 10 (2024) e37444, https://doi.org/10.1016/j.heliyon.2024.e37444.

[42] A.S. Kalamdhad, A.A. Kazmi, Effects of turning frequency on compost stability and some chemical characteristics in a rotary drum composter, Chemosphere 74 (2009) 1327–1334, https://doi.org/10.1016/j.chemosphere.2008.11.058.

[43] Z. Jiang-ming, Effect of turning frequency on co-composting pig manure and fungus residue, J. Air Waste Manage. Assoc. 67 (2017) 313–321, https://doi.org/10.1080/10962247.2016.1232666.

[44] R. Parkinson, P. Gibbs, S. Burchett, T. Misselbrook, Effect of turning regime and seasonal weather conditions on nitrogen and phosphorus losses during aerobic composting of cattle manure, Bioresour. Technol. 91 (2004) 171–178, https://doi.org/10.1016/S0960-8524(03)00174-3.